

Robust Inference-Time Steering of Protein Diffusion Models via Embedding Optimization

Minhuan Li¹ Jiequn Han¹ Pilar Cossio¹ Luhuan Wu¹

Abstract

In many biophysical inverse problems, the goal is to generate biomolecular conformations that are both physically plausible and consistent with experimental measurements. As recent sequence-to-structure diffusion models provide powerful data-driven priors, posterior sampling has emerged as a popular framework by guiding atomic coordinates to target conformations using experimental likelihoods. However, when the target lies in a low-density region of the prior, posterior sampling requires aggressive and brittle weighting of the likelihood guidance. Motivated by this limitation, we propose *EmbedOpt*, an alternative inference-time approach for steering diffusion models to optimize experimental likelihoods in the conditional embedding space. As this space encodes rich sequence and coevolutionary signals, optimizing over it effectively shifts the diffusion prior to align with experimental constraints. We validate *EmbedOpt* on two benchmarks simulating cryo-electron microscopy map fitting and experimental distance constraints. We show that *EmbedOpt* outperforms the coordinate-based posterior sampling method in map fitting tasks, matches performance on distance constraint tasks, and exhibits superior engineering robustness across hyperparameters spanning two orders of magnitude. Moreover, its smooth optimization behavior enables a significant reduction in the number of diffusion steps required for inference, leading to better efficiency.

1. Introduction

Biomolecules are dynamic systems that undergo conformational changes in order to perform their biological functions. Consequently, identifying the ensemble of relevant conformations accessible to a biomolecule is essential for

¹Flatiron Institute. Correspondence to: Minhuan Li <minhuanli@flatironinstitute.org>, Luhuan Wu <lwu@flatironinstitute.org>.

Preprint. February 6, 2026.

understanding its functional mechanisms. However, inferring these conformations from experimental observables constitutes a challenging inverse problem. This difficulty arises from the high dimensionality of conformational space, which is intrinsically hard to sample, and from the need to simultaneously enforce physical realism while maintaining agreement with experimental data. Traditionally, this problem has been addressed using physics-based force fields combined with stepwise sampling under the maximum entropy principle (Rieping et al., 2005). Although powerful, such approaches are computationally demanding and often require extensive, labor-intensive refinement to adequately explore alternative conformational states that match both the physics and data (Croll, 2018).

A recent paradigm shift in the field leverages pretrained generative models as data-driven priors to regularize the conformational search. State-of-the-art protein sequence-to-structure generative models such as AlphaFold 3 (Abramson et al., 2024) predominantly use a conditional diffusion module (Song et al., 2020; Ho et al., 2020) for structure generation after sequence processing. In contrast to AlphaFold 2, which performs static structure prediction (Jumper et al., 2021), the diffusion module enables *distributional* modeling of biomolecular 3D coordinates x_0 conditioned on sequence information c by iteratively refining noisy structures x_t through a series of diffusion steps, starting from random noise. While these generative models capture dominant structural modes with remarkable accuracy, solving structure-determination inverse problems often requires recovering specific conformational states that lie outside the high-probability regions of the pretrained model. Addressing this limitation necessitates the incorporation of additional constraints—derived from experimental measurements or other desired properties—that were not present during training. Viewed through a Bayesian lens, the AlphaFold 3 framework naturally accommodates this integration by interpreting the pretrained diffusion model as a sequence-conditioned prior $p(x_0 | c)$ while experimental measurements y define a likelihood $p(y | x_0)$, yielding a posterior distribution $p(x_0 | y, c) \propto p(x_0 | c)p(y | x_0)$.

Because the exact diffusion posterior is intractable, Diffusion Posterior Sampling (DPS) (Chung et al., 2022) and

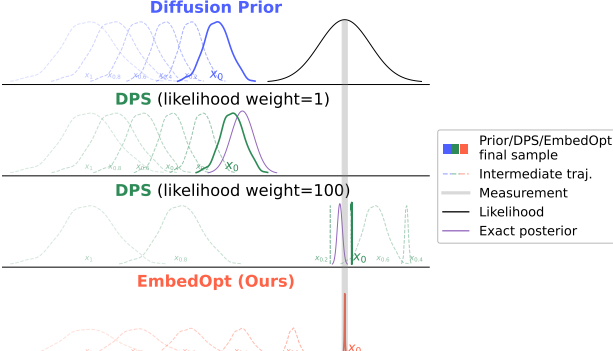


Figure 1. Synthetic illustration comparing DPS and EmbedOpt under prior-likelihood mismatch. The diffusion prior has limited overlap with the measurement likelihood (**top**). With a likelihood weight = 1 (controlled by α_t in Eq. (7)), the posterior is distant from the measurement (**second**). Upweighting the likelihood (**third**) moves the posterior toward the measurement but leads to an ill-conditioned sampling landscape. In contrast, EmbedOpt (**bottom**) iteratively updates the prior during sampling, progressively correcting the initial prior misspecification and enabling samples to concentrate near the measurement. All curves are shown as smoothed histograms. See Appendix C for more details.

many subsequent methods provide a practical approximation by applying likelihood-gradient guidance to intermediate noisy coordinates x_t , progressively steering samples toward high-likelihood regions. In practice, this guidance is scaled by a tunable factor that effectively reweights the likelihood relative to the diffusion prior. DPS-style approaches have been successfully applied to recover protein conformations from cryo-electron microscopy (cryo-EM) maps and NOE spectroscopy data (Maddipatla et al., 2025; Raghu et al., 2025). However, performance is highly sensitive to the choice of likelihood weighting, a phenomenon also observed in image inverse problems (He et al., 2023; Zach et al., 2025). Without careful tuning, this balance is brittle: strong likelihood guidance often produces unphysical conformations, whereas weak guidance remains close to the prior and fails to satisfy experimental constraints. This sensitivity is further exacerbated under prior–likelihood mismatch. As illustrated in Figure 1, when the pretrained prior assigns little probability mass to high-likelihood regions, DPS fails to generate measurement-consistent samples unless the likelihood is aggressively upweighted. Such upweighting, however, induces an ill-conditioned sampling landscape. Similar behavior has been observed in real systems: Raghu et al. (2025) report that models such as AlphaFold 3 and Boltz-1 (Wohlwend et al., 2025) produce samples concentrated around a single dominant conformation. When experimental data favor alternative structures, this concentration of prior mass leads to a mismatch, rendering posterior sampling unstable and require a delicate likelihood guidance schedule.

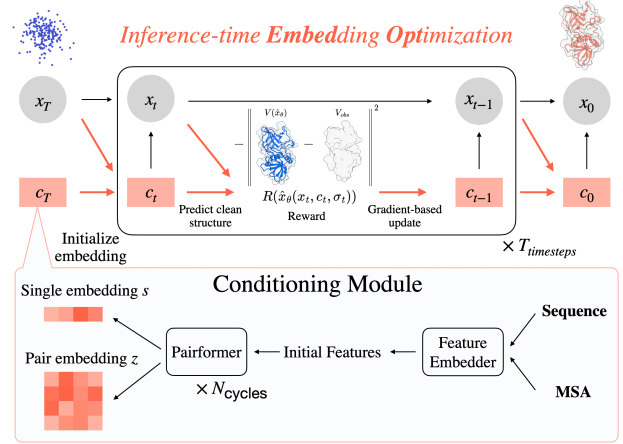


Figure 2. Schematic of Inference-Time Embedding Optimization (EmbedOpt). Experimental measurements like Cryo-EM maps provide rich conformational information that may not correspond to dominant modes of pretrained prediction models. EmbedOpt adapts a pretrained diffusion model at inference time by maximizing an experimental likelihood reward $R(\cdot)$. (Top) **In a single forward pass**, the conditional embedding is iteratively updated ($c_t \rightarrow c_{t-1}$) using gradients from the denoised structure \hat{x}_θ , greedily increasing the reward along the denoise trajectory. (Bottom) While applicable to general conditional frameworks, we use an AlphaFold 3-style backbone where the Conditioning Module serves as an embedder of coevolutionary information, processing sequence and MSA inputs to generate the initial embedding c_T .

To overcome these limitations, we developed *EmbedOpt*, a robust inference-time method that reduces prior–likelihood mismatch by optimizing the sequence embedding c , effectively reshaping the diffusion prior to better align with the experimental constraints. As shown for the toy example in Figure 1-bottom, EmbedOpt adapts the diffusion prior by updating the prior location parameter c , producing final samples concentrated around the measurement. In Alphafold 3-style protein diffusion models, the sequence embedding c encodes rich *semantic* information, derived from inputs such as multiple sequence alignments (MSA), which strongly shapes the prior distribution over atomic conformations. Because this embedding governs the model’s structural preferences, modifying it effectively reshapes the conformational prior. EmbedOpt exploits this property by formulating inverse structure determination as a reward optimization problem, in which experimental constraints define the reward. At inference time, our method performs lightweight, greedy optimization of the conditional embedding via single-step gradient ascent at each diffusion step, promoting alignment between the induced prior and experimental data without altering model parameters. This strategy preserves the model’s inherent structural regularization while maintaining efficiency compared to model fine-tuning. A schematic of our method is provided in Figure 2.

We implement EmbedOpt based on the Protenix model

(ByteDance AML AI4Science Team et al., 2025), an open-source PyTorch reproduction of AlphaFold 3. We validate EmbedOpt using two distinct benchmark tasks designed to simulate common structure determination inverse problems: optimizing correlation to a cryo-EM map and satisfying residue pair distance constraints derived from nuclear magnetic resonance (NMR) measurements. Our results demonstrate three key advantages. i) **Improved or competitive performance**: In map correlation tasks, EmbedOpt achieves higher *best-achieved* performance than DPS (both methods tuned via hyperparameter sweeps), particularly on “hard” targets (initial correlation < 0.5). In distance constraint tasks, EmbedOpt and DPS achieve similar best-achieved performance. ii) **Robustness**: EmbedOpt is much less sensitive to hyperparameter choice compared to DPS, demonstrating a broad hyperparameter stability plateau spanning by two orders of magnitudes. iii) **Efficiency**: EmbedOpt maintains stable optimization and high generation quality despite a significant reduction in diffusion steps.

2. Background

Diffusion Models. Diffusion models (Ho et al., 2020; Song et al., 2020) are powerful generative models that sample from a target distribution $p(x_0)$ through an iterative process. We consider the probability flow ODE formulation (Karras et al., 2022)

$$dx_t = -\dot{\sigma}(t)\sigma(t)\nabla_{x_t} \log p_t(x_t) dt \quad (1)$$

where $\sigma(t)$ is a noise level increasing in t with $\sigma(0) = 0$, $p_t(x_t) = \int p(x_0)\mathcal{N}(x_t|x_0, \sigma(t)^2) dx_0$ is the time-dependent marginal distribution, and $\nabla_{x_t} \log p_t(x_t)$ is the score function. The idea of diffusion models is that starting from $x_T \sim \mathcal{N}(0, \sigma_T^2 \mathbb{I})$ for some large σ_T , integrating this ODE backward in time recovers target samples $x_0 \sim p(x_0)$. While the score is typically intractable, it can be approximated using a *denoiser* network $\hat{x}_\theta(x_t, \sigma(t))$ trained to predict the posterior mean $\mathbb{E}[x_0 | x_t]$. Tweedie’s formula (Efron, 2011) yields an approximation of the score $\nabla_{x_t} \log p_t(x_t) \approx [\hat{x}_\theta(x_t, \sigma(t)) - x_t]/\sigma^2(t)$. With a learned denoiser, we numerically integrate Eq. (1) backward on a discrete time grid $\tau_T > \dots > \tau_0 = 0$. With a slight abuse of notation, we write $x_t := x_{\tau_t}$ and $\sigma_t := \sigma(\tau_t)$ for $t \in \{0, \dots, T\}$. An Euler step from τ_t to τ_{t-1} gives

$$x_{t-1} \approx x_t + \eta_t(\hat{x}_\theta(x_t, \sigma_t) - x_t), \quad (2)$$

where $\eta_t := \frac{\Delta\sigma_t}{\sigma_t} = \frac{\sigma_t - \sigma_{t-1}}{\sigma_t}$.

Protein Sequence-to-Structure Diffusion Models. Recent protein sequence-to-structure prediction models like AlphaFold 3 introduce a conditional diffusion head to predict a distribution $p(x_0 | c)$ of structures x_0 from sequence information c . This conditional diffusion is realized by designing the denoiser \hat{x}_θ in Eq. (2) to accept additional input

c such that it is written as $\hat{x}_\theta(x_t, c, \sigma_t)$. As illustrated in Figure 2, conditional embeddings are computed from the sequence and MSA information, which encodes coevolutionary signals. In this work, we focus on the conditioning inputs $c = \{s, z\}$, where the *single* embedding s and *pair* embedding z are produced by the PairFormer module which capture *residue-wise* and *residue-pair* interactions, respectively. Conditioning the diffusion process on these embeddings anchors a strongly informed prior over protein structures, ensuring that generated structures remain consistent with the evolutionary constraints of the target sequence. Additional conditioning inputs, such as initial features and optional template structures, are considered as fixed context and we omit them in the following notations.

3. Method

Setup. We consider a conditional protein diffusion model that defines a prior distribution over 3D structures $x_0 \in \mathbb{R}^{N_{\text{res}} \times 3}$, conditioned on sequence embeddings $c = \{s, z\}$, where single embedding $s \in \mathbb{R}^{N_{\text{res}} \times C_s}$ and pair embedding $z \in \mathbb{R}^{N_{\text{res}} \times N_{\text{res}} \times C_z}$. Here N_{res} denotes the number of residues in the input sequence, and C_s and C_z denote the channel dimensions of single and pair embeddings. For many inverse problems, we can prescribe an experimental likelihood $p(y | x_0)$ given some measurement y of the underlying structure x_0 . We define a reward function $R(x_0) \propto \log p(y | x_0)$ ¹ and for simplicity we omit the dependence on y . We assume R is differentiable, as is the case in many applications. Our goal is to generate structures x_0 with high reward while maintaining physical plausibility.

3.1. EmbedOpt: Objective and Main Algorithm

Given an initial sample x_T and embedding c , the diffusion model produces a final sample $x_0(x_T, c)$ as a function of x_T and c , which can be stochastic due to the additional noise injection in the sampling scheme. For a fixed x_T , the *oracle global objective* to optimize the embedding c is $\arg \max_c R(x_0(x_T, c))$. Directly optimizing this objective via gradient-based methods would require backpropagating through the entire sampling trajectory, which can be memory-intensive or numerically unstable. To address this challenge, we adopt a dynamic optimization strategy over the sampling path. Given an intermediate sample x_t at step t , we consider a *surrogate local objective*:

$$\arg \max_c R(\hat{x}_\theta(x_t, c, \sigma_t)). \quad (3)$$

That is, we optimize the reward evaluated at the denoising prediction given the current sample x_t and noise level σ_t , which we call the *surrogate reward*. As $\sigma_t \rightarrow 0$ the surro-

¹Since our goal is to maximize the reward, scaling the log likelihood does not influence the optimum.

Algorithm 1 EmbedOpt

```

1: Input: differentiable reward function  $R$ , original conditional embedding  $c$ , denoiser network  $\hat{x}_\theta$ , adaptive learning rate  $\alpha_t$ , total steps  $T$ , noise schedule  $\{\sigma_t\}_{t=0}^T$ 
2: Output: final sample  $x_0$ 
3: Initialize embedding  $c_T \leftarrow c$ 
4: Sample initial coordinate  $x_T \sim \mathcal{N}(0, \sigma_T^2)$ 
5: for  $t = T, T-1, \dots, 1$  do
6:   Make denoised prediction  $\hat{x}_0 \leftarrow \hat{x}_\theta(x_t, c_t, \sigma_t)$ 
7:   Update embedding  $c_{t-1} \leftarrow c_t + \alpha_t \nabla_{c_t} R(\hat{x}_0)$ 
8:   Update coord.  $x_{t-1} \leftarrow x_t + \eta_t [\hat{x}_\theta(x_t, c_{t-1}, \sigma_t) - x_t]$ 
     where  $\eta_t = \frac{\sigma_t - \sigma_{t-1}}{\sigma_{t-1}}$ 
9: end for

```

gate reward is closer to the true reward value of the final x_0 . This relaxation is in the spirit of those used in prior diffusion posterior sampling works (e.g. Chung et al., 2022).

In practice, we perform greedy, inference-time optimization by taking a single gradient step on the surrogate objective in Eq. (3) at each diffusion step. This procedure dynamically adapts the prior while simultaneously steering the sampling trajectory to higher surrogate reward region. Algorithm 1 summarizes the procedure of EmbedOpt. We initialize the embedding $c_T = c$ with the pretrained model’s original conditioning inputs, and then iteratively update c_t . At each step t , we compute the denoising prediction $\hat{x}_0 = \hat{x}_\theta(x_t, c_t, \sigma_t)$ using the current embedding c_t . We then evaluate the surrogate reward $R(\hat{x}_0)$ and take a gradient ascent step to obtain c_{t-1} . The updated embedding c_{t-1} is subsequently used both to advance the diffusion process to x_{t-1} and to initialize the embedding optimization for the next time step. Repeating this procedure yields the final sample x_0 .

Gradient Normalization. While Algorithm 1 (Line 7) assumes an adaptive learning rate α_t , in practice we normalize the gradient by its root mean squared (RMS) value and use a constant base learning rate α , which is effective and simplifies tuning. In particular, we apply the gradient normalization for the single and pair embeddings separately:

$$(g_{s_t}, g_{z_t}) := (\nabla_{s_t} R(\hat{x}_0), \nabla_{z_t} R(\hat{x}_0)) = \nabla_{c_t} R(\hat{x}_0),$$

$$\bar{g}_{s_t} = \frac{g_{s_t}}{\sqrt{\frac{1}{d_s} \sum_{i=1}^{d_s} (g_{s_t}^{(i)})^2}}, \quad \bar{g}_{z_t} = \frac{g_{z_t}}{\sqrt{\frac{1}{d_z} \sum_{i=1}^{d_z} (g_{z_t}^{(i)})^2}},$$

where $d_s = N_{\text{res}} \times C_s$, $d_z = N_{\text{res}} \times N_{\text{res}} \times C_z$ are the dimensions of single and pair embeddings, respectively. Then embeddings are updated with RMS-normalized gradients

$$s_{t-1} = s_t + \alpha \bar{g}_{s_t}, \quad z_{t-1} = z_t + \alpha \bar{g}_{z_t}. \quad (4)$$

The complete algorithm with this normalized-gradient update is given in Algorithm 2, which is also adapted to the stochastic sampling scheme used in AlphaFold 3.

3.2. Theoretical Analysis

Although EmbedOpt operates as a dynamic optimization procedure, we show that it yields monotonic improvement of the surrogate reward under suitable regularity and trust-region assumptions, which can be achieved by choosing sufficiently small step size $\Delta\sigma_t$ and learning rate α . Denote $F(x, c, \sigma) := R(\hat{x}_\theta(x, c, \sigma))$ the surrogate reward given (x, c, σ) . The following guarantee of surrogate reward improvement for EmbedOpt holds:

Proposition 1 (Informal). *For a fixed (x_t, c_t, σ_t) , consider the transition to $(x_{t-1}, c_{t-1}, \sigma_{t-1})$ under the EmbedOpt update (Algorithm 1, Line 6-8). Assume F is locally smooth and \hat{x}_θ is bounded in a neighborhood of (x_t, c_t, σ_t) . The following bound holds*

$$F(x_{t-1}, c_{t-1}, \sigma_{t-1}) \geq F(x_t, c_t, \sigma_t) + \frac{\alpha_t}{2} \|g_{c_t}\|^2 - \Delta\sigma_t [G_x \sigma_t^{-1} (\|\hat{x}_\theta(x_t, c_{t-1}, \sigma_t) - x_t\|) + G_\sigma] \quad (5)$$

where $g_{c_t} = \nabla_{c_t} F(x_t, c_t, \sigma_t)$ and G_x and G_σ are Lipschitz constants depending on (x_t, c_t, σ_t) .

Moreover, if the learning rate $0 \leq \alpha_t \leq \alpha_{\max}$ and the noise level step size $0 \leq \Delta\sigma_t \leq \Delta_{\max}$, where constants $\alpha_{\max}, \Delta_{\max}$ depend on (x_t, c_t, σ_t) , the surrogate reward is non-decreasing: $F(x_{t-1}, c_{t-1}, \sigma_{t-1}) \geq F(x_t, c_t, \sigma_t)$. (see a formal statement and proof in Appendix A.2).

This proposition shows that EmbedOpt is a local trust-region method: when the learning rate α_t and noise-level step size $\Delta\sigma_t$ are sufficiently small, the update remains in a neighborhood where the first-order ascent guarantee holds, leading to a non-decreasing surrogate reward. The quantitative bound in Eq. (5) makes it explicit. The reward improvements arises from the gradient-ascent gain $\frac{\alpha_t}{2} \|g_{c_t}\|^2$, which dominates the potential deviation due to the coordinate and noise-level updates, i.e. the second line in Eq. (5), within the trust region. When the gradient is zero, the first-order improvement term vanishes and the trust-region condition becomes vacuous. This corresponds to a local optimum of the surrogate reward and the embedding will stay unchanged at that step.

3.3. Comparison to DPS

As DPS is a primary baseline in this work, we briefly summarize its formulation and present an algorithmic comparison to our method (see detailed background in Appendix B.1). DPS frames inverse problems as sampling from the posterior of the form $p(x_0 \mid c) \exp\{R(x_0)\}$ (with c held fixed) which can be simulated using the *likelihood-guided* ODE,

$$\begin{aligned} dx_t = -\dot{\sigma}(t)\sigma(t) & \left[\nabla_{x_t} \log p_t(x_t) \right. \\ & \left. + \nabla_{x_t} \log \mathbb{E} [\exp\{R(x_0)\} \mid x_t] \right] dt, \end{aligned}$$

where the intractable conditional expectation is approximated by $\log \mathbb{E} [\exp\{R(x_0)\} \mid x_t] \approx R(\hat{x}_\theta(x_t, c, \sigma_t))$.

Using a tuning parameter α_t that controls the likelihood guidance strength, DPS’s discrete-step update is

$$x_{t-1} = x_t + \eta_t(\hat{x}_0 - x_t + \alpha_t \nabla_{x_t} R(\hat{x}_0)), \quad (6)$$

where $\hat{x}_0 := \hat{x}_\theta(x_t, c, \sigma_t)$. For notational consistency, we refer to α_t also as an adaptive learning rate, whose value may differ from our choice in EmbedOpt.

By chain rule, DPS’s update in Eq. (6) can be re-written as

$$x_{t-1} = x_t + \eta_t(\hat{x}_0 - x_t + \alpha_t J_{x_t}^\top \nabla_{\hat{x}_0} R(\hat{x}_0)) \quad (7)$$

where J_{x_t} is the Jacobian of \hat{x}_0 with respect to x_t .

For EmbedOpt, we apply a first-order Taylor approximation to rewrite its update rule (Algorithm 1, Line 6-8; see Appendix A.3 derivation) in a similar fashion

$$x_{t-1} \approx x_t + \eta_t [\hat{x}_0 - x_t + \alpha_t J_{c_t} J_{c_t}^\top \nabla_{\hat{x}_0} R(\hat{x}_0)] \quad (8)$$

where J_{c_t} is the Jacobian of \hat{x}_0 with respect to c_t .

Comparing Eq. (7) and Eq. (8), while we observe a structural similarity that both methods leverage the *denoising reward gradient* $\nabla_{\hat{x}_0} R(\hat{x}_0)$ to guide diffusion sampling, a substantial geometric difference arises: in DPS, the reward gradient is pulled back to the noisy coordinate x_t through $J_{x_t}^\top$, which couples the update direction to the local sensitivity of the denoiser with respect to x_t . In contrast, EmbedOpt introduces a preconditioning operator $J_{c_t} J_{c_t}^\top$ on the denoising reward gradient, yielding an update that reflects the geometry induced by the embedding c_t . As a result, the coordinate update remains within the span of the reward gradient, while its magnitude and anisotropy are modulated by the embedding geometry. This difference suggests a possible behavioral distinction: DPS may be sensitive to the conditioning of the noisy coordinate space, whereas EmbedOpt may exhibit more stable optimization dynamics and reduced sensitivity to the learning rate. In § 5, we empirically observe these behaviors and leverage their differences to achieve practical efficiency gains with EmbedOpt.

4. Related Works

Machine-Learning Methods for Solving Structure-Determination Inverse Problems. Most closely related is Maddipatla et al. (2025) and Raghu et al. (2025) that formulate inverse problems as a posterior sampling task under a pretrained diffusion prior and operate within a DPS-style framework. Maddipatla et al. (2025) infers conformational ensembles, i.e. multiple conformational states corresponding to the same protein sequence, from ensemble-averaged experiment data. Raghu et al. (2025) focuses on the cryo-EM application, introducing a multi-scale guidance strategy

which applies global structural constraints in early sampling stage and local constraints in later stage. Parallel efforts in the deterministic AlphaFold 2 era, such as Fadini et al. (2025), explored optimizing latent coevolutionary embeddings to align predictions with experimental measurements. Other strategies integrate constraints through parameter-wise fine-tuning (Xie et al., 2025; Stahl et al., 2023; Zhang et al., 2025) or specialized architectures like ModelAngelo (Jamali et al., 2024). Compared to prior approaches, EmbedOpt directly shifts the distribution via embedding optimization to align with experimental data, avoiding the manifold deviation risks in coordinate-based steering and the computational cost of parameter-wise model fine-tuning.

Exploration of Alternative Conformations. An adjacent line of research is to sample diverse conformational states of protein structures. While existing sequence-to-structure deep learning models exhibit limited diversity, an exploratory line of research seeks to simulate alternative conformations by subsampling or perturbing the MSA inputs (Wayment-Steele et al., 2024; Kalakoti & Wallner, 2025; Lee et al., 2025; Del Alamo et al., 2022). More recently, Richman et al. (2025) propose an inference-time diffusion sampling algorithm in AlphaFold 3-style models that generate conformations as a prescribed distance away from a reference structure, using a combination of DPS and particle filtering methods (Wu et al., 2023). Our current work focuses on generating conformations consistent with experimental constraints by adapting a pretrained conditional diffusion model. In principle, this framework can be applied to sample alternative conformations when an appropriate objective, such as promoting diversity, is defined.

General Diffusion Inference-Time Steering. Beyond the biomolecular context, a broad class of methods steer diffusion models at inference time toward different objectives. At one end are widely used guidance-based techniques, such as classifier-free guidance (Ho & Salimans, 2022) or DPS for inverse problems (Chung et al., 2022). At the opposite extreme are methods that require additional training (e.g. Domingo-Enrich et al., 2025), offering stronger adaptation at higher computational cost. Between these lies a middle ground of training-free but more sophisticated inference-time methods, such as sequential Monte Carlo-based approaches (Wu et al., 2023; Ren et al., 2025). A distinct avenue is prompt-tuning, which steers generation by optimizing prompts as conditions and has been primarily explored in text-to-image diffusion models to maximize image-level rewards (Hao et al., 2023; Chung et al., 2023). While related in spirit, these approaches typically rely on iterative embedding optimization or reinforcement learning, leading to substantially higher computational cost. In contrast, our method performs a single embedding update per diffusion step, resulting in a significantly simpler and more efficient

inference procedure tailored to protein diffusion models.

5. Experiments

Solving biomolecular inverse problems requires reconciling fidelity to experimental signals with adherence to physical laws. To evaluate our method and compare against baselines, we design two benchmarks that simulate real-world structure determination scenarios: (i) fitting to a cryo-EM density map and (ii) satisfying residue-pair distance constraints, as obtained from NMR or other experimental measurements. The tasks probe challenging regimes where experimental targets lie far from the pretrained model’s dominant mode.

Experiment Protocol. Our experiments are based on the Protenix model which serves as the diffusion prior. We compare our method against DPS and the prior model.

Following the implementation of [Maddipatla et al. \(2025\)](#), we apply a gradient normalization for DPS, which effectively sets the adaptive learning rate α_t in Eq. (6) to

$$\alpha_t = \alpha \|\hat{x}_\theta(x_t, c, \sigma_t) - x_t\| / \|\nabla_{x_t} R(\hat{x}_\theta(x_t, c, \sigma_t))\|,$$

where $\|\cdot\|$ denotes the l_2 norm, and α is a constant base learning rate. See the full DPS algorithm in Algorithm 4.

Similarly, under the normalization strategy used in EmbedOpt (Eq. (4)), the adaptive learning rate α_t regarding the single and pair embedding components s_t and z_t is

$$\begin{aligned} \alpha_t[s_t] &= \alpha / \text{RMS}(\nabla_{s_t} R(\hat{x}_\theta(x_t, c_t, \sigma_t))), \\ \alpha_t[z_t] &= \alpha / \text{RMS}(\nabla_{z_t} R(\hat{x}_\theta(x_t, c_t, \sigma_t))), \end{aligned}$$

where RMS is root-mean-square and α is constant w.r.t. t .

Although the normalization strategies differ across methods, they place DPS and EmbedOpt in a relatively comparable optimization regime. We therefore vary only the base learning rate α over a similar range for both methods, where we observe both methods traverse from underfitting reward to overfitting within the same numerical range of α .

We perform energy relaxation using a classical force field to the generated structures by EmbedOpt and DPS to fix potential local geometry issues, following [Maddipatla et al. \(2025\)](#). Energy relaxation is not applied to samples from the prior model. For each experiment setting, we run 3 random seeds. See Appendix D for all experiment details.

5.1. Cryo-EM Map Fitting

In single-particle cryo-EM, 3D density maps are reconstructed from processed and filtered 2D projection images. A typical downstream task in cryo-EM is building an atomic model, starting from an existing PDB deposition or prediction model, to maximize agreement between the model-derived and experimental maps. To simulate Cryo-EM map

fitting problem, we assemble a diverse set of 77 protein systems from PDB with high resolution structures (<4.5 Å) and low sequence similarity (25%). We generate synthetic target Cryo-EM maps V_{obs} at 5.0 Å resolution from those systems using SFC_Torch ([Li et al., 2025](#)), with atomic B-factors uniformly set to 50 Å² to standardize thermal variation. Similarly, we can define a differentiable forward model to generate map $V(x_0)$ given a structure x_0 .

The reward $R(x_0) = -\frac{1}{N_x N_y N_z} \sum_{N_x, N_y, N_z} (V(x_0) - V_{obs})^2$ is defined as the negative mean squared error between the normalized target map V_{obs} and the normalized rendered map $V(x_0)$, where $V(x_0), V_{obs} \in \mathbb{R}^{N_x \times N_y \times N_z}$, and N_x, N_y, N_z are grid size. Performance is assessed in two aspects: (i) map correlation, denoted by cc , using `phenix.validation_cryoem` ([Afonine et al., 2018](#)) and (ii) physical plausibility quantified by Molprobity score using `phenix.molprobity` ([Williams et al., 2018](#)).

Figure 3a exemplifies a challenging target, 8H1I, where the pretrained prior model generates a conformation with incorrect domain orientation ($cc=0.42$) relative to reference map. For this case, DPS fails to correct this topology, stagnating at a local optimum ($cc=0.58$) even under the best hyperparameters tested. In contrast, EmbedOpt successfully resolves the global domain rearrangement, yielding a structure that closely matches the ground truth density ($cc=0.93$). More examples are shown in Figure 5.

Improved Performance in Low-Density Prior Regimes.

To systematically quantify this advantage, we compare the best-achieved performance (after sweeping learning rates) across the full dataset (Figure 3b). We define task “difficulty” as $1 - \text{prior map correlation value}$, which is a proxy for the misalignment between the prior’s dominant mode and the experimental target. While both methods perform comparably on “easy” targets (difficulty < 0.4) where the prior is already well-aligned, EmbedOpt consistently outperforms DPS on “hard” targets. This confirms that optimizing the conditioning embedding allows the model to access low-probability regions of the prior conformational landscape that are effectively inaccessible to direct coordinate steering.

Engineering Robustness and Manifold Stability. Beyond the best-achieved performance, EmbedOpt demonstrates superior engineering robustness (Figure 3c) compared to DPS. DPS, as a posterior sampling method, involves an inherent “tug-of-war” between the prior and the likelihood: low learning rates provide insufficient likelihood guidance, while high learning rates push the trajectory off the data manifold, resulting in unphysical structures (Figure 6). Consequently, DPS requires delicate hyperparameter tuning to find the narrow efficacy window. Conversely, by treating the generative model as a parametric manifold of valid structures, EmbedOpt mitigates this fragility. It exhibits a stable performance plateau across learning rates spanning two or-

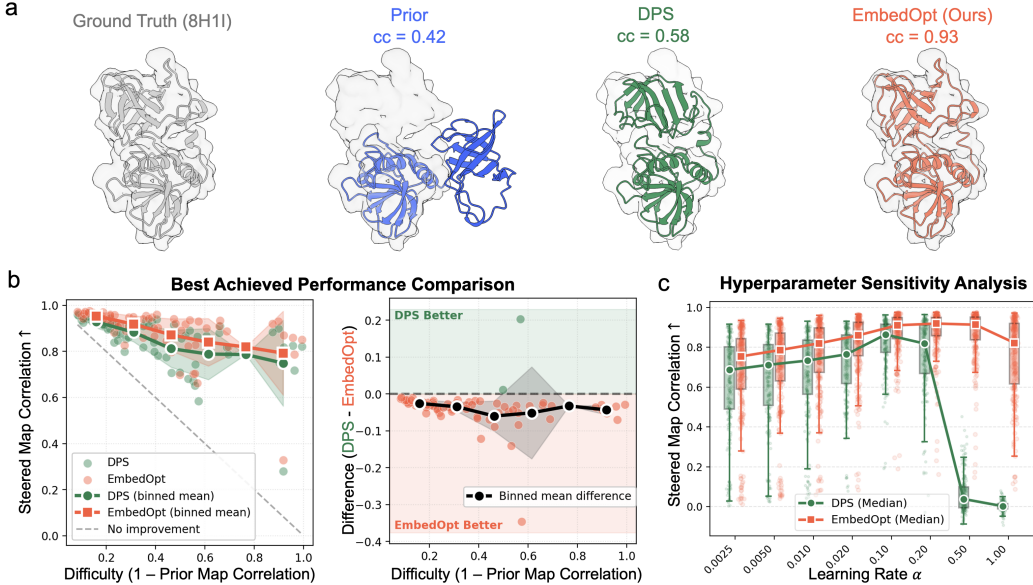


Figure 3. Cryo-EM Map Fitting Benchmark. (a) **Visualization of a challenging target:** 8H1I requires significant inter-domain rearrangement of the prior structure ($cc = 0.42$) to fit the target density map (gray volume), DPS remains trapped in a local optimum ($cc = 0.58$), and EmbedOpt successfully reorients the domains ($cc = 0.93$). cc is the map correlation coefficient. (b) **Best-achieved Performance vs. Task Difficulty:** (left) Best-sampled structures (from 7 learning rates $\times 3$ random seeds) across 77 systems (dots), binned by task difficulty (1 - map correlation of the prior model). Mean and standard deviation are calculated in each bin. EmbedOpt maintains an advantage especially on harder targets (> 0.4). (right) The difference plot shows EmbedOpt outperforming DPS across the majority of systems. (c) **Hyperparameter Sensitivity:** Distribution of map correlations across all systems for varying learning rates. Box plots span the interquartile range (25th-75th percentile) with the median highlighted. Whiskers extend to $1.5 \times$ IQR. Individual data are shown as semi-transparent dots. DPS exhibits a brittle “sweet spot” due to the tug-of-war between guidance strength and structural validity controlled by learning rate. EmbedOpt maintains high performance across learning rates spanning two orders of magnitude.

ders of magnitude (0.01 to 1.0), achieving on average higher performance than DPS while substantially reducing the cost of hyperparameter search in practice. This stability extends to stereochemical quality, where EmbedOpt maintains valid geometries (low MolProbity scores) even at large learning rates where DPS fails (Figure 7).

5.2. Experimental Distance-Constrained Structure Determination

Experimental techniques, such as NMR and chemical cross-linking, often yield sparse pairwise distance constraints, posing a critical inverse problem of inferring conformations consistent with these geometric bounds. To simulate such problems, we ensemble a benchmark of 24 multi-domain protein systems from Zhang et al. (2025) as they include flexible inter-domain orientations that challenge existing generative models. Constraints are derived by identifying the top $K = 20$ residue pairs with the largest structural discrepancies between the ground truth and the prior model’s predictions, with a $\delta = 2.0$ Å tolerance to the target value. The reward function is formulated as $R(x_0) = -\sum_{i=1}^K \min(|d_i(x_0)| - |d_i^{\text{target}}|, \delta)^2$, where $d_i(x_0)$ is the residue-pair distance in x_0 corresponding to the i -th constrained pair, and d_i^{target} is the respective target

distance. Performance is measured by the # of satisfied constraints, and stereochemical quality by MolProbity score.

Performance Summary. Both EmbedOpt and DPS have comparable best-achieved performance in this task (Figure 8a). Unlike Cryo-EM map fitting where the unimodal likelihood requires specific global rearrangements and is often misaligned with the prior, sparse distance targets offer more flexible constraints, allowing both methods to saturate the reward. However, consistent with the map task, EmbedOpt exhibits superior robustness, maintaining valid geometries across a much wider learning rate spectrum (Figure 8b).

Although both methods perform well in their optimal regimes, practical utility also depends on inference stability and efficiency. We examine these aspects in following.

Smoother Reward Optimization Trace. We analyze the optimization dynamics to understand the inference stability under the default $T = 200$ diffusion steps. Figure 4 reveals a striking contrast: while DPS suffers from high-frequency volatility, EmbedOpt exhibits a smooth, monotonic improvement of the reward. We observe this optimization stability across test systems. This observation is consistent with Proposition 1, which suggests that EmbedOpt empirically operate within a well-behaved trust-region of the optimiza-

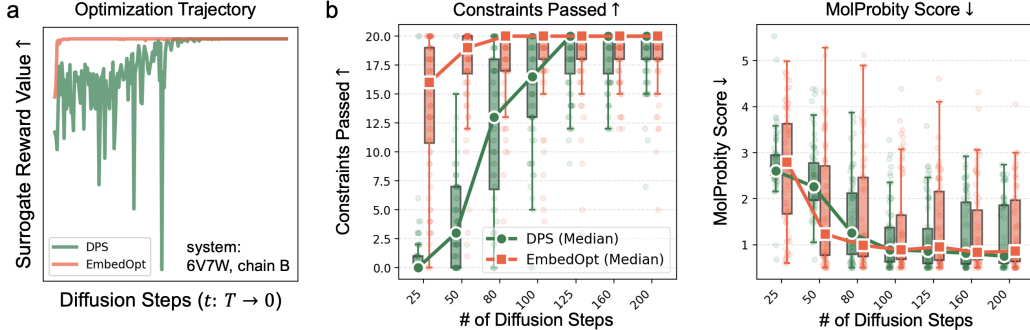


Figure 4. Distance Constraint Benchmark. (a) **Optimization Trajectory:** Representative surrogate reward traces for system 6V7W show EmbedOpt increases surrogate reward smoothly and monotonically to the optimum, while DPS has high-frequency volatility. (b) **Step-Efficiency Scaling:** We substantially reduce # of diffusion steps from 200 down to 20 while keeping the base learning rate $\alpha \times \#$ of steps = const., where const. is picked with $\alpha = 0.1$ at 200 steps, an optimal choice for both methods based on Figure 8b. **Left:** With sufficient diffusion steps (200), both methods satisfy nearly all constraints; however, DPS performance deteriorates sharply below 100 steps, whereas EmbedOpt maintains a median constraint satisfaction rate above 75%. **Right:** EmbedOpt preserves good stereochemical quality (MolProbity score < 2) as diffusion steps are reduced fourfold (200 → 50), while DPS degrades substantially below 100 steps.

tion dynamics. We hypothesized that this superior stability would translate into practical efficiency by permitting larger optimization step sizes.

Robust Performance with Reduced Diffusion Steps. To test this hypothesis, we perform an efficiency scaling experiment on the distance constraint task ($K = 20$). Starting from a 200-step baseline (with the base learning rate $\alpha = 0.1$, optimal for both methods as indicated in Figure 8b), we reduce the diffusion steps while proportionally increasing learning rates to maintain a constant total guidance magnitude (base learning rate \times # of steps = const.). As shown in Figure 4b, EmbedOpt demonstrates remarkable resilience to this scaling, maintaining near-optimal constraint satisfaction (median constraints passed ≈ 20) down to 50 diffusion steps—a 4× speedup over the baseline. Conversely, DPS performance collapses below 100 steps as high learning rates destabilize coordinate updates. Crucially, this efficiency gain retains structural validity; EmbedOpt maintains excellent MolProbity scores (<2.0) even in the low-step regime, confirming that the accelerated optimization remains on the valid manifold.

6. Discussion

In this work, we introduce EmbedOpt, an inference-time method steering biomolecular sequence-to-structure diffusion models by optimizing conditional embeddings. We show that EmbedOpt matches or outperforms DPS while offering greater robustness and efficiency across multiple structure-determination inverse problems.

Although we present EmbedOpt primarily for optimizing single conformations, it naturally extends to multi-conformation objectives for two distinct purposes. First, many biophysical measurements, including NMR and

single-particle cryo-EM, may encode distributional constraints. By optimizing a shared embedding over batches of samples, EmbedOpt can infer conformational ensembles whose collective properties match experimental observations. Second, batch-based embedding optimization reduces variance from individual samples, producing a more robust consensus prior that favors high-reward regions. This naturally enables a two-stage strategy in which EmbedOpt first shifts the prior toward the likelihood, after which DPS or other guidance techniques are applied locally, avoiding brittle cold-start coordinate steering.

The success of EmbedOpt relies on the assumption that the embedding space from the pretrained model induces a structural manifold that covers the target conformation. When sequence information is limited (e.g. shallow MSAs) or when the target structure involves physical interactions absent from the training data, EmbedOpt can overfit: the generated structures satisfy the experimental constraints but lack physical validity. Although we mitigate this issue with post-processing energy relaxation, future work could incorporate similar regularization directly during EmbedOpt inference. More broadly, this observation sheds light on the design of next-generation biomolecular generative models: rather than treating the conditioning module purely as a feature extractor, training objectives should explicitly regularize the embedding space (e.g. via variational bottlenecks) to ensure it forms a smooth, navigable manifold suitable for inference-time optimization.

7. Acknowledgment

The authors thank Alisia Fadini, Colin Kalicki, and Tetiana Parshakova for valuable discussions.

References

Abramson, J., Adler, J., Dunger, J., Evans, R., Green, T., Pritzel, A., Ronneberger, O., Willmore, L., Ballard, A. J., Bambrick, J., et al. Accurate structure prediction of biomolecular interactions with alphafold 3. *Nature*, 630 (8016):493–500, 2024.

Afonine, P. V., Klaholz, B. P., Moriarty, N. W., Poon, B. K., Sobolev, O. V., Terwilliger, T. C., Adams, P. D., and Urzhumtsev, A. New tools for the analysis and validation of cryo-em maps and atomic models. *Biological Crystallography*, 74(9):814–840, 2018.

ByteDance AML AI4Science Team, Chen, X., Zhang, Y., Lu, C., Ma, W., Guan, J., Gong, C., Yang, J., Zhang, H., Zhang, K., Wu, S., Zhou, K., Yang, Y., Liu, Z., Wang, L., Shi, B., Shi, S., and Xiao, W. Proteinix - advancing structure prediction through a comprehensive alphafold3 reproduction. *bioRxiv*, 2025. doi: 10.1101/2025.01.08.631967.

Chung, H., Kim, J., Mccann, M. T., Klasky, M. L., and Ye, J. C. Diffusion posterior sampling for general noisy inverse problems. *arXiv preprint arXiv:2209.14687*, 2022.

Chung, H., Ye, J. C., Milanfar, P., and Delbracio, M. Prompt-tuning latent diffusion models for inverse problems. *arXiv preprint arXiv:2310.01110*, 2023.

Croll, T. I. Isolde: a physically realistic environment for model building into low-resolution electron-density maps. *Biological Crystallography*, 74(6):519–530, 2018.

Del Alamo, D., Sala, D., Mchaourab, H. S., and Meiler, J. Sampling alternative conformational states of transporters and receptors with alphafold2. *Elife*, 11:e75751, 2022.

Domingo-Enrich, C., Drozdal, M., Karrer, B., and Chen, R. T. Q. Adjoint matching: Fine-tuning flow and diffusion generative models with memoryless stochastic optimal control. In *ICLR*, 2025.

Efron, B. Tweedie’s formula and selection bias. *Journal of the American Statistical Association*, 106(496):1602–1614, 2011.

Fadini, A., Li, M., McCoy, A. J., Terwilliger, T. C., Read, R. J., Hekstra, D., and AlQuraishi, M. Alphafold as a prior: Experimental structure determination conditioned on a pretrained neural network. *bioRxiv*, pp. 2025–02, 2025.

Hao, Y., Chi, Z., Dong, L., and Wei, F. Optimizing prompts for text-to-image generation. *Advances in Neural Information Processing Systems*, 36:66923–66939, 2023.

He, Y., Murata, N., Lai, C.-H., Takida, Y., Uesaka, T., Kim, D., Liao, W.-H., Mitsufuji, Y., Kolter, J. Z., Salakhutdinov, R., et al. Manifold preserving guided diffusion. *arXiv preprint arXiv:2311.16424*, 2023.

Ho, J. and Salimans, T. Classifier-free diffusion guidance. *arXiv preprint arXiv:2207.12598*, 2022.

Ho, J., Jain, A., and Abbeel, P. Denoising diffusion probabilistic models. *Advances in neural information processing systems*, 33:6840–6851, 2020.

Jamali, K., Käll, L., Zhang, R., Brown, A., Kimanius, D., and Scheres, S. H. Automated model building and protein identification in cryo-em maps. *Nature*, 628(8007):450–457, 2024.

Jumper, J., Evans, R., Pritzel, A., Green, T., Figurnov, M., Ronneberger, O., Tunyasuvunakool, K., Bates, R., Žídek, A., Potapenko, A., et al. Highly accurate protein structure prediction with alphafold. *nature*, 596(7873):583–589, 2021.

Kalakoti, Y. and Wallner, B. Afsample2 predicts multiple conformations and ensembles with alphafold2. *Communications Biology*, 8(1):373, 2025.

Karras, T., Aittala, M., Aila, T., and Laine, S. Elucidating the design space of diffusion-based generative models. *Advances in neural information processing systems*, 35: 26565–26577, 2022.

Lee, M., Schafer, J. W., Prabakaran, J., Chakravarty, D., Clore, M. F., and Porter, L. L. Large-scale predictions of alternative protein conformations by alphafold2-based sequence association. *Nature Communications*, 16(1): 5622, 2025.

Li, M., Dalton, K., and Hekstra, D. Sfcalculator: connecting deep generative models and crystallography. *BioRxiv*, 2025.

Maddipatla, A., Sellam, N. B., Bojan, M., Vedula, S., Schanda, P., Marx, A., and Bronstein, A. M. Inverse problems with experiment-guided alphafold. *arXiv preprint arXiv:2502.09372*, 2025.

Ponder, J. W. and Case, D. A. Force fields for protein simulations. *Advances in protein chemistry*, 66:27–85, 2003.

Prince, E. *International Tables for Crystallography, Volume C: Mathematical, physical and chemical tables*. Springer Science & Business Media, 2004.

Raghu, R., Levy, A., Wetzstein, G., and Zhong, E. D. Multiscale guidance of protein structure prediction with heterogeneous cryo-EM data. In *The Thirty-ninth Annual*

Conference on Neural Information Processing Systems, 2025.

Ren, Y., Gao, W., Ying, L., Rotskoff, G. M., and Han, J. Driftlite: Lightweight drift control for inference-time scaling of diffusion models. *arXiv preprint arXiv:2509.21655*, 2025.

Richman, D. D., Karaguesian, J., Suomivuori, C.-M., and Dror, R. O. Unlocking hidden biomolecular conformational landscapes in diffusion models at inference time. *arXiv preprint arXiv:2512.03312*, 2025.

Rieping, W., Habeck, M., and Nilges, M. Inferential structure determination. *Science*, 309(5732):303–306, 2005.

Song, Y., Sohl-Dickstein, J., Kingma, D. P., Kumar, A., Ermon, S., and Poole, B. Score-based generative modeling through stochastic differential equations. *arXiv preprint arXiv:2011.13456*, 2020.

Stahl, K., Graziadei, A., Dau, T., Brock, O., and Rapp-silber, J. Protein structure prediction with in-cell photo-crosslinking mass spectrometry and deep learning. *Nature Biotechnology*, 41(12):1810–1819, 2023.

Wayment-Steele, H. K., Ojoawo, A., Otten, R., Apitz, J. M., Pitsawong, W., Hömberger, M., Ovchinnikov, S., Colwell, L., and Kern, D. Predicting multiple conformations via sequence clustering and alphafold2. *Nature*, 625(7996):832–839, 2024.

Williams, C. J., Headd, J. J., Moriarty, N. W., Prisant, M. G., Videau, L. L., Deis, L. N., Verma, V., Keedy, D. A., Hintze, B. J., Chen, V. B., et al. Molprobity: more and better reference data for improved all-atom structure validation. *Protein Science*, 27(1):293–315, 2018.

Wohlwend, J., Corso, G., Passaro, S., Getz, N., Reveiz, M., Leidal, K., Swiderski, W., Atkinson, L., Portnoi, T., Chinn, I., et al. Boltz-1 democratizing biomolecular interaction modeling. *BioRxiv*, pp. 2024–11, 2025.

Wu, L., Trippe, B., Naesseth, C., Blei, D., and Cunningham, J. P. Practical and asymptotically exact conditional sampling in diffusion models. *Advances in Neural Information Processing Systems*, 36:31372–31403, 2023.

Xie, Y., Zhang, C., Li, S., Du, X., Lu, Y., Wang, M., Hu, Y., Chen, Z., Liu, S., and Gao, Y. Q. Integrating diverse experimental information to assist protein complex structure prediction by grasp. *Nature Methods*, 22(11):2362–2374, 2025.

Zach, M., Haouchat, Y., and Unser, M. A statistical benchmark for diffusion posterior sampling algorithms. *arXiv preprint arXiv:2509.12821*, 2025.

Zhang, Y., Zhang, Z., Kagaya, Y., Terashi, G., Zhao, B., Xiong, Y., and Kihara, D. Distance-af improves predicted protein structure models by alphafold2 with user-specified distance constraints. *Communications Biology*, 8(1):1392, 2025.

Algorithm 2 Embed-Opt Adapted for AlphaFold 3 Sampling Scheme

```

1: Input: differentiable reward function  $R$ , original conditional embedding  $c = \{z, s\}$ , denoiser network  $\hat{x}_\theta$ , base reward learning rate  $\alpha$ , total steps  $T$ , noise schedule  $\{\sigma_t\}_{t=0}^T$ , minimum noise amplification level  $\gamma_0 = 1.0$ , noise amplification factor  $\gamma = 0.8$ , noise scale  $\rho = 1.003$ , step scale  $\eta = 1.5$ 
2: Output: final sample  $x_0$ 
3: Initialize embedding  $c_T \leftarrow c$ 
4: Sample initial coordinate  $x_T \sim \mathcal{N}(0, \sigma_T^2)$ 
5: for  $t = T, T-1, \dots, 1$  do
6:   if  $\sigma_{t-1} > \gamma_{\min}$  then
7:     Add noise to coordinate  $x_t \leftarrow x_t + \rho \sqrt{(\gamma + 1)^2 - 1} \sigma_t \epsilon_t$ ,  $\epsilon_t \sim \mathcal{N}(0, \mathbb{I})$ 
8:     Amplify noise level  $\sigma_t \leftarrow (\gamma + 1) \sigma_t$ 
9:   end if
10:  Make denoised prediction  $\hat{x}_0 \leftarrow \hat{x}_\theta(x_t, \textcolor{red}{c_t} = (s_t, z_t), \sigma_t)$ 
11:  Compute gradient  $g_{ct} \leftarrow [g_{st}, g_{zt}]$  where  $g_{st} \leftarrow \nabla_{s_t} R(\hat{x}_0)$  and  $g_{zt} \leftarrow \nabla_{z_t} R(\hat{x}_0)$ 
12:  Normalize gradient by RMS  $\bar{g}_{ct} \leftarrow [\bar{g}_{st}, \bar{g}_{zt}]$  where  $\bar{g}_{st} \leftarrow \frac{g_{st}}{\sqrt{\frac{1}{d_s} \sum_{i=1}^{d_s} (g_{st}^{(i)})^2}}$  and  $\bar{g}_{zt} \leftarrow \frac{g_{zt}}{\sqrt{\frac{1}{d_z} \sum_{i=1}^{d_z} (g_{zt}^{(i)})^2}}$ 
13:  Update embedding  $\textcolor{red}{c_{t-1}} \leftarrow c_t + \alpha \bar{g}_{ct}$ 
14:  Update coordinate  $x_{t-1} \leftarrow x_t + \eta_t [\hat{x}_\theta(x_t, \textcolor{red}{c_{t-1}}, \sigma_{t-1}) - x_t]$  where  $\eta_t = \frac{\sigma_t - \sigma_{t-1}}{\sigma_t} * \eta$ 
15: end for

```

A. Method Details

A.1. EmbedOpt Algorithm Adapted to AlphaFold 3 Sampling Scheme

The original sampler in AlphaFold 3 adopts the stochastic sampling scheme proposed by [Karras et al. \(2022\)](#), which injects a small amount of noise into the coordinates x_t at the initial steps (Lines 6–9) until a minimum noise level is reached. It further employs a step scale of $\eta = 1.5$ to increase the diffusion step size (Line 14). Protenix, as an open-source reproduction of AlphaFold 3, uses the same settings.

We present the full EmbedOpt algorithm, compatible with AlphaFold 3-style sampling scheme, in Algorithm 2. We adopt the same default hyperparameters in all protein benchmark experiments.

Finally, note that when setting $\gamma = 0$ and step scale $\eta = 1$ in Algorithm 2, it recovers the deterministic sampler in Algorithm 1 with a standard diffusion step size.

A.2. Proposition on the Monotone Surrogate Reward Improvement of EmbedOpt

We provide a formal statement and proof of Proposition 1.

Setup. Define the surrogate reward at (x_t, c_t, σ_t) ,

$$F(x_t, c_t, \sigma_t) := R(\hat{x}_\theta(x_t, c_t, \sigma_t)). \quad (9)$$

EmbedOpt's update at step t is

$$c_{t-1} = c_t + \alpha_t \nabla_{c_t} F(x_t, c_t, \sigma_t) \quad (10)$$

$$x_{t-1} = x_t + \sigma_t^{-1} \Delta \sigma_t (\hat{x}_\theta(x_t, c_{t-1}, \sigma_t) - x_t), \quad (11)$$

where $\Delta \sigma_t := \sigma_t - \sigma_{t-1} > 0$ is the noise level step size.

Assumption 1 (Local c -smoothness of F). *Given (x_t, c_t, σ_t) , there exists a neighborhood \mathcal{C} of c_t with a radius r_c such that $\forall c, c' \in \mathcal{C}$, the function $c \mapsto F(x_t, c, \sigma_t)$ is L_c -smooth:*

$$F(x_t, c', \sigma_t) \geq F(x_t, c, \sigma_t) + \nabla_c F(x_t, c, \sigma_t)^\top (c' - c) - \frac{L_c}{2} \|c' - c\|^2. \quad (12)$$

where $\mathcal{C}, r_c > 0, L_c > 0$ depend on (x_t, c_t, σ_t) .

Assumption 2 (Local c -boundedness of \hat{x}_θ). *For the given $(x_t, \mathcal{C}, \sigma_t)$ in Assumption 1, $\max_{c \in \mathcal{C}} \|\hat{x}_\theta(x_t, c, \sigma_t)\| \leq \|\hat{x}_\theta\|_{\infty, \mathcal{C}}$ for some constant $\|\hat{x}_\theta\|_{\infty, \mathcal{C}}$ depending on $(x_t, \mathcal{C}, \sigma_t)$.*

Assumption 3 (Local x -Lipschitz continuity of F). *For the given $(x_t, \mathcal{C}, \sigma_t)$ in Assumption 1, there exists a neighborhood \mathcal{X} of x_t with a radius r_x such that $\forall x, x' \in \mathcal{X}, \forall c \in \mathcal{C}$, the map $x \mapsto F(x, c, \sigma_t)$ is G_x -Lipschitz:*

$$|F(x', c, \sigma_t) - F(x, c, \sigma_t)| \leq G_x \|x' - x\|, \quad (13)$$

where $\mathcal{X}, r_x > 0, G_x > 0$ depend on $(x_t, \mathcal{C}, \sigma_t)$.

Assumption 4 (Local σ -Lipschitz continuity). *For the given $(\mathcal{X}, \mathcal{C}, \sigma_t)$ in Assumptions 1 and 3, there exists a maximum step size $r_\sigma > 0$ such that $\forall x \in \mathcal{X}, \forall c \in \mathcal{C}, \forall \sigma$ such that $0 \leq \sigma_t - \sigma \leq r_\sigma$, the map $\sigma \mapsto F(x, c, \sigma)$ is G_σ -Lipschitz:*

$$|F(x, c, \sigma) - F(x, c, \sigma_t)| \leq G_\sigma (\sigma_t - \sigma) \quad (14)$$

where $r_\sigma > 0, G_\sigma > 0$ depend on $(\mathcal{X}, \mathcal{C}, \sigma_t)$.

Proposition 2 (EmbedOpt one-step surrogate reward improvement). *Given (x_t, c_t, σ_t) , under Assumptions 1, 3 and 4, if the EmbedOpt learning rate α_t satisfies*

$$0 < \alpha_t \leq \alpha_{\max} := \min\left\{\frac{1}{L_c}, \frac{r_c}{\|\nabla_{c_t} F(x_t, c_t, \sigma_t)\|}\right\} \quad (15)$$

and the noise level step size $\Delta\sigma_t = \sigma_t - \sigma_{t-1}$ satisfies

$$\begin{aligned} \Delta\sigma_t \leq \Delta_{\max} := \min\{ & \left[\sigma_t^{-1} G_x (\|\hat{x}_\theta\|_{\infty, \mathcal{C}} + \|x_t\|) + G_{\sigma_t} \right]^{-1} \frac{\alpha_t}{2} \|\nabla_{c_t} F(x_t, c_t, \sigma_t)\|^2, \\ & \frac{\sigma_t r_x}{\|\hat{x}_\theta\|_{\infty, \mathcal{C}} + \|x_t\|}, r_\sigma \} \end{aligned} \quad (16)$$

then the surrogate reward under the EmbedOpt update Eqs. (10) and (11) is non-decreasing across time:

$$F(x_{t-1}, c_{t-1}, \sigma_{t-1}) \geq F(x_t, c_t, \sigma_t). \quad (17)$$

Moreover, the quantitative bound holds

$$F(x_{t-1}, c_{t-1}, \sigma_{t-1}) \geq F(x_t, c_t, \sigma_t) + \frac{\alpha_t}{2} \|\nabla_{c_t} F(x_t, c_t, \sigma_t)\|^2 - G_x \frac{\Delta\sigma_t}{\sigma_t} \|\hat{x}_\theta(x_t, c_{t-1}, \sigma_t) - x_t\| - G_\sigma \Delta\sigma_t. \quad (18)$$

Remarks.

- Assumptions 1 to 4 are on the smoothness and boundedness of the surrogate reward $F(\cdot, \cdot, \cdot)$ in a neighborhood of (x_t, c_t, σ_t) , which hold for sufficiently regular denoiser network $\hat{x}_\theta(\cdot, \cdot, \cdot)$ and the reward function $R(\cdot)$.
- The learning rate requirement for α_t in Eq. (15) is a classical gradient ascent condition, satisfied for sufficiently small α_t . This assumption ensures that the embedding update yields non-negative reward improvement within a trust region.
- The assumption on the noise level step size $\Delta\sigma_t$ in Eq. (16) is another trust-region assumption which ensures the reward gain by updating embedding dominates the worst-case surrogate reward decrease due to $x_t \rightarrow x_{t-1}$ and $\sigma_t \rightarrow \sigma_{t-1}$. Noticeably, when the embedding gradient $\nabla_{c_t} F(x_t, c_t, \sigma_t) \neq 0$, we can pick sufficiently small noise level step size $\Delta\sigma_t$ for this assumption to hold. However, if c_t is a local optimum with $\nabla_{c_t} F(x_t, c_t, \sigma_t) = 0$, this assumption is vacuous and there is no reward ascent guarantee against the shift caused by coordinate and noise level updates.

Proof We first evaluate the surrogate reward gain from the embedding update $c_t \rightarrow c_{t-1}$ in Step 1, for a sufficiently small learning rate α_t in Eq. (15). Then we compute the reward lower bound while updating $x_t \rightarrow x_{t-1}$ in Step 2 and $\sigma_t \rightarrow \sigma_{t-1}$ in Step 3. Finally, under the step-size assumption in Eq. (16), we prove the non-decreasing surrogate reward given a full update from (x_t, c_t, σ_t) to $(x_{t-1}, c_{t-1}, \sigma_{t-1})$ in Step 4, which leads to Eqs. (17) and (18).

Step 1: gain from embedding update $c_t \rightarrow c_{t-1}$ given fixed x_t and σ_t . When the learning rate $\alpha_t \leq \frac{r_c}{\|\nabla_{c_t} F(x_t, c_t, \sigma_t)\|}$ (implied by Eq. (15)), we have $\|c_{t-1} - c_t\| = \alpha_t \|\nabla_{c_t} F(x_t, c_t, \sigma_t)\| \leq r_c$, and hence $c_{t-1} \in \mathcal{C}$ (recall \mathcal{C} is defined as the neighborhood of c_t with a radius r_c).

By Assumption 1 with $(c, c') = (c_t, c_{t-1}) \in \mathcal{C}$,

$$F(x_t, c_{t-1}, \sigma_t) \geq F(x_t, c_t, \sigma_t) + \nabla_{c_t} F(x_t, c_t, \sigma_t)^\top (c_{t-1} - c_t) - \frac{L_c}{2} \|c_{t-1} - c_t\|^2. \quad (19)$$

Using $c_{t-1} - c_t = \alpha_t \nabla_{c_t} F(x_t, c_t, \sigma_t)$,

$$F(x_t, c_{t-1}, \sigma_t) \geq F(x_t, c_t, \sigma_t) + \alpha_t \left(1 - \frac{L_c \alpha_t}{2}\right) \|\nabla_{c_t} F(x_t, c_t, \sigma_t)\|^2. \quad (20)$$

If $0 < \alpha_t \leq 1/L_c$, then $1 - \frac{L_c \alpha_t}{2} \geq \frac{1}{2}$, hence

$$F(x_t, c_{t-1}, \sigma_t) \geq F(x_t, c_t, \sigma_t) + \frac{\alpha_t}{2} \|\nabla_{c_t} F(x_t, c_t, \sigma_t)\|^2. \quad (21)$$

Step 2: reward lower bound from coordinate update $x_t \rightarrow x_{t-1}$ given fixed c_{t-1} and σ_t . Note that

$$\|x_{t-1} - x_t\| = \Delta \sigma_t \sigma_t^{-1} \|\hat{x}_\theta(x_t, c_{t-1}, \sigma_t) - x_t\| \quad (22)$$

$$\leq \Delta \sigma_t \sigma_t^{-1} (\|\hat{x}_\theta(x_t, c_{t-1}, \sigma_t)\| + \|x_t\|) \quad (23)$$

$$\leq \Delta \sigma_t \sigma_t^{-1} (\|\hat{x}_\theta\|_{\infty, \mathcal{C}} + \|x_t\|) \quad (24)$$

where the last line follows from Assumption 2.

When the noise-level step size $\Delta \sigma_t \leq \frac{\sigma_t r_x}{\|\hat{x}_\theta\|_{\infty, \mathcal{C}} + \|x_t\|}$ implied by Eq. (16), we have that $\|x_{t-1} - x_t\| \leq r_x$ and hence $x_{t-1} \in \mathcal{X}$ (recall \mathcal{X} is defined as the neighborhood of x_t with a radius r_x).

By Assumption 3 with $(x, x') = (x_t, x_{t-1}) \in \mathcal{X}$,

$$F(x_{t-1}, c_{t-1}, \sigma_t) \geq F(x_t, c_{t-1}, \sigma_t) - G_x \|x_{t-1} - x_t\|. \quad (25)$$

Using $x_{t-1} - x_t = \sigma_t^{-1} \Delta \sigma \|\hat{x}_\theta(x_t, c_{t-1}, \sigma_t) - x_t\|$, we have

$$F(x_{t-1}, c_{t-1}, \sigma_t) \geq F(x_t, c_{t-1}, \sigma_t) - \sigma_t^{-1} G_x \Delta \sigma_t \|\hat{x}_\theta(x_t, c_{t-1}, \sigma_t) - x_t\|. \quad (26)$$

Step 3: reward lower bound from noise level update $\sigma_t \rightarrow \sigma_{t-1}$ given fixed x_{t-1} and c_{t-1} . By Assumption 4 with $(\sigma, \sigma') = (\sigma_t, \sigma_{t-1})$ (satisfied when $\Delta \sigma_t \leq r_\sigma$ by Eq. (16)),

$$F(x_{t-1}, c_{t-1}, \sigma_{t-1}) \geq F(x_{t-1}, c_{t-1}, \sigma_t) - G_\sigma \Delta \sigma_t. \quad (27)$$

Step 4: full update Combining Eqs. (21), (26) and (27),

$$F(x_{t-1}, c_{t-1}, \sigma_{t-1}) \geq F(x_{t-1}, c_{t-1}, \sigma_t) - G_\sigma \Delta \sigma_t \quad (28)$$

$$\geq F(x_t, c_{t-1}, \sigma_t) - \sigma_t^{-1} G_x \Delta \sigma_t \|\hat{x}_\theta(x_t, c_{t-1}, \sigma_t) - x_t\| - G_\sigma \Delta \sigma_t \quad (29)$$

$$\geq F(x_t, c_t, \sigma_t) + \frac{\alpha_t}{2} \|\nabla_{c_t} F(x_t, c_t, \sigma_t)\|^2 - \sigma_t^{-1} G_x \Delta \sigma_t \|\hat{x}_\theta(x_t, c_{t-1}, \sigma_t) - x_t\| - G_\sigma \Delta \sigma_t \quad (30)$$

The last line recovers the bound in Eq. (18).

When the noise level also satisfies the following trust region as part of the condition in Eq. (16):

$$\Delta \sigma_t \leq [\sigma_t^{-1} G_x (\|\hat{x}_\theta\|_{\infty, \mathcal{C}} + \|x_t\|) + G_{\sigma_t}]^{-1} \frac{\alpha_t}{2} \|\nabla_{c_t} F(x_t, c_t, \sigma_t)\|^2, \quad (31)$$

which implies

$$\frac{\alpha_t}{2} \|\nabla_{c_t} F(x_t, c_t, \sigma_t)\|^2 - \sigma_t^{-1} G_x \Delta \sigma_t \|\hat{x}_\theta(x_t, c_{t-1}, \sigma_t) - x_t\| - G_\sigma \Delta \sigma_t \geq 0, \quad (32)$$

we have the non-decreasing surrogate reward for a full EmbedOpt update across time:

$$F(x_{t-1}, c_{t-1}, \sigma_{t-1}) \geq F(x_t, c_t, \sigma_t). \quad (33)$$

■

A.3. Derivation of the First-order Taylor Approximation to the EmbedOpt Update in Eq. (8)

We apply a first-order Taylor approximation of $\hat{x}_\theta(x_t, c_{t-1}, \sigma_t)$ around c_t :

$$\hat{x}_\theta(x_t, c_{t-1}, \sigma_t) \approx \hat{x}_\theta(x_t, c_t, \sigma_t) + J_{c_t}(c_{t-1} - c_t) \quad (34)$$

where the remainder is $o(\|c_{t-1} - c_t\|)$, and $J_{c_t} := \nabla_{c_t} \hat{x}_\theta(x_t, c_t, \sigma_t)$.

Using the embedding update rule, i.e. $c_{t-1} - c_t = \alpha_t \nabla_{c_t} R(\hat{x}_\theta(x_t, c_t, \sigma_t))$,

$$\hat{x}_\theta(x_t, c_{t-1}, \sigma_t) \approx \hat{x}_\theta(x_t, c_t, \sigma_t) + \alpha_t J_{c_t}^\top \nabla_{c_t} R(\hat{x}_\theta(x_t, c_t, \sigma_t)) \quad (35)$$

Applying chain rule to $\nabla_{c_t} R(\hat{x}_\theta(x_t, c_t, \sigma_t))$ and write $\hat{x}_0 = \hat{x}_\theta(x_t, c_t, \sigma_t)$,

$$\hat{x}_\theta(x_t, c_{t-1}) \approx \hat{x}_\theta(x_t, c_t, \sigma_t) + \alpha_t J_{c_t} J_{c_t}^\top \nabla_{\hat{x}_0} R(\hat{x}_0). \quad (36)$$

Finally, EmbedOpt's full one-step update of $x_t \rightarrow x_{t-1}$ can be approximated by

$$x_{t-1} = x_t + \eta_t [\hat{x}_\theta(x_t, c_{t-1}, \sigma_t) - x_t] \quad (37)$$

$$\approx x_t + \eta_t [\hat{x}_\theta(x_t, c_t, \sigma_t) + \alpha_t J_{c_t} J_{c_t}^\top \nabla_{\hat{x}_0} R(\hat{x}_0) - x_t], \quad (38)$$

which recovers Eq. (8).

B. Diffusion Posterior Sampling and Applications to Biophysical Inverse Problems

B.1. DPS Background

Diffusion posterior sampling (DPS, Chung et al., 2022) is a popular approach for solving inverse problems by leveraging diffusion models as flexible priors in a Bayesian posterior sampling framework. Consider a likelihood of the form $p^R(x_0) \propto \exp\{R(x_0)\}$ where $R(\cdot)$ is a reward function that encodes alignments with experimental measurement. Given a diffusion model prior $p(x_0 | c)$, DPS aims to (approximately) sample from the resulting posterior which is proportional to $p(x_0 | c) \exp\{R(x_0)\}$.

To sample from the posterior, the probability flow ODE in Eq. (1) is modified to include the additional gradient term of the log expected exponentiated reward, which is referred to as *likelihood guidance*,

$$dx_t = -\dot{\sigma}(t) \sigma(t) \left[\nabla_{x_t} \log p_t(x_t) + \nabla_{x_t} \log \mathbb{E} [\exp\{R(x_0)\} | x_t] \right] dt \quad (39)$$

While intractable, DPS approximates the log expected exponentiated reward by the reward evaluated at the posterior expectation

$$\log \mathbb{E} [\exp\{R(x_0)\} | x_t] \approx \log \exp\{R(\mathbb{E}[x_0 | x_t])\} = R(\mathbb{E}[x_0 | x_t]). \quad (40)$$

Using the denoising prediction $\hat{x}_\theta(x_t, c, \sigma_t) \approx \mathbb{E}[x_0 | x_t]$, DPS's discrete-time update is given by

Algorithm 3 Diffusion Posterior Sampling (DPS, Chung et al., 2022)

```

1: Input: differentiable reward function  $R$ , original conditional embedding  $c$ , denoiser network  $\hat{x}_\theta$ , adaptive learning rate  $\alpha_t$ , total steps  $T$ , noise schedule  $\{\sigma_t\}_{t=0}^T$ 
2: Output: final sample  $x_0$ 
3: Sample initial coordinate  $x_T \sim \mathcal{N}(0, \sigma_T^2)$ 
4: for  $t = T, T-1, \dots, 1$  do
5:   Make denoised prediction  $\hat{x}_0 \leftarrow \hat{x}_\theta(x_t, c, \sigma_t)$ 
6:   Update coordinate  $x_{t-1} \leftarrow x_t + \eta_t [\hat{x}_0 - x_t + \alpha_t \nabla_{x_t} R(\hat{x}_0)]$  where  $\eta_t = \frac{\sigma_t - \sigma_{t-1}}{\sigma_t}$ 
7: end for

```

Algorithm 4 DPS Adapted for AlphaFold 3 Sampling Scheme

```

1: Input: differentiable reward function  $R$ , original conditional embedding  $c = \{z, s\}$ , denoiser network  $\hat{x}_\theta$ , base reward learning rate  $\alpha$ , total steps  $T$ , noise schedule  $\{\sigma_t\}_{t=0}^T$ , minimum noise amplification level  $\gamma_0 = 1.0$ , noise amplification factor  $\gamma = 0.8$ , noise scale  $\rho = 1.003$ , step scale  $\eta = 1.5$ 
2: Output: final sample  $x_0$ 
3: Sample initial coordinate  $x_T \sim \mathcal{N}(0, \sigma_T^2)$ 
4: for  $t = T, T-1, \dots, 1$  do
5:   if  $\sigma_{t-1} > \gamma_{\min}$  then
6:     Add noise to coordinate  $x_t \leftarrow x_t + \rho \sqrt{(\gamma + 1)^2 - 1} \sigma_t \epsilon_t$ ,  $\epsilon_t \sim \mathcal{N}(0, \mathbb{I})$ 
7:     Amplify noise level  $\sigma_t \leftarrow (\gamma + 1) \sigma_t$ 
8:   end if
9:   Make denoised prediction  $\hat{x}_0 \leftarrow \hat{x}_\theta(x_t, c, \sigma_t)$ 
10:  Compute gradient  $g_{x_t} \leftarrow \nabla_{x_t} R(x_0)$ 
11:  Normalize gradient  $\bar{g}_{x_t} \leftarrow \|\hat{x}_0 - x_t\| \frac{g_{x_t}}{\|g_{x_t}\|}$ 
12:  Update coordinate  $x_{t-1} \leftarrow x_t + \eta_t [\hat{x}_\theta(x_t, c, \sigma_t) - x_t + \alpha \bar{g}_{x_t}]$  where  $\eta_t = \frac{\sigma_t - \sigma_{t-1}}{\sigma_t} * \eta$ 
13: end for

```

$$x_{t-1} = x_t + (\sigma_t - \sigma_{t-1}) \sigma_t \left[\frac{\hat{x}_\theta(x_t, c, \sigma_t) - x_t}{\sigma_t^2} + \nabla_{x_t} R(\hat{x}_\theta(x_t, c, \sigma_t)) \right] \quad (41)$$

$$= x_t + \underbrace{\frac{\sigma_t - \sigma_{t-1}}{\sigma_t}}_{:= \eta_t} [\hat{x}_\theta(x_t, c, \sigma_t) - x_t + \sigma_t^2 \nabla_{x_t} R(\hat{x}_\theta(x_t, c, \sigma_t))]. \quad (42)$$

In practice, using an adaptive ‘‘learning rate’’ schedule α_t that controls the likelihood guidance strength can be helpful,

$$x_{t-1} = x_t + \eta_t (\hat{x}_\theta(x_t, \sigma_t) - x_t + \alpha_t \nabla_{x_t} R(\hat{x}_\theta(x_t, \sigma_t))). \quad (43)$$

The optimal learning rate schedule would depend on specific downstream tasks.

Connection to Reweighting Likelihood. Setting $\alpha_t = \sigma_t^2 w$ admits a Bayesian interpretation in which the likelihood is reweighted by a factor of w relatively to the prior, with the targeted posterior $\propto p(x_0) \exp\{wR(x_0)\}$. Since DPS is only an approximate inference method, this interpretation should be viewed as heuristic rather than exact.

Generic DPS Algorithm. We summarize the DPS algorithm with a generic learning rate schedule α_t and under a standard ODE sampling scheme in Algorithm 3.

B.2. DPS Algorithm Adapted to AlphaFold 3 Sampling Scheme

We follow the gradient normalization strategy in Maddipatla et al. (2025) (official implementation can be found in https://github.com/sai-advaith/guided_alphaFold, which is also built on the Protenix model), and summarize the DPS algorithm adapted for AlphaFold 3 sampling scheme in Algorithm 4.

C. Details on Synthetic Illustration in Figure 1

In the synthetic example in Figure 1, we consider a diffusion prior model to be a 1-dimensional Gaussian $p(x_0 | c) = \mathcal{N}(x_0 | c, 0.5^2)$ conditioned on the location parameter $c = 5$. We set the diffusion noise schedule $\sigma(t) = t$ for $t \in [0, 1]$. Since $p(x_0 | c)$ is Gaussian, we can access the conditional expectation $\mathbb{E}[x_0 | x_t] \forall (x_t, t)$ without training a denoiser network.

The measurement likelihood is given by $\mathcal{N}(y | x_0, 1)$ with the measurement $y = 20$. This setting simulates the case where the prior model has low probability mass on the experimental measurements.

We run the unguided prior model sampling, DPS, and EmbedOpt using $T = 1,000$ uniform timesteps over $[0, 1]$.

To connect likelihood reweighting and the DPS’s learning rate (as discussed in Appendix B.1), we set $\alpha_t = \sigma_t^2 w$ in Algorithm 3 where w is a weighting parameter. More concretely,

- When $w = 1$, the exact posterior $p(y | x_0, c) \propto \mathcal{N}(x_0 | c, 0.5^2) \mathcal{N}(y | x_0, 1)$, and the DPS update is $x_{t-1} = x_t + \eta_t [\hat{x}_\theta(x_t, c, \sigma_t) - x_t + \sigma_t^2 \nabla_{x_t} \log N(y | \mathbb{E}[x_0 | x_t], 1)]$.
- When $w = 100$, the exact posterior is $p(y_0 | x_0, c) \propto \mathcal{N}(x_0 | c, 0.5^2) \mathcal{N}(y | x_0, 1)^w$, and the DPS update is $x_{t-1} = x_t + \eta_t [\hat{x}_\theta(x_t, c, \sigma_t) - x_t + \sigma_t^2 100 \nabla_{x_t} \log N(y | \mathbb{E}[x_0 | x_t], 1)]$.

The EmbedOpt results in Figure 1 are obtained from running Algorithm 1 with $\alpha_t = \alpha \frac{1}{\|\nabla_{c_t} R(\hat{x}_0)\|}$ and $\alpha = 0.1$. In practice we found a range of α from 0.05 to 5 to work well, that is, to be able to maximize the log likelihood.

D. Experiment details

D.1. Post-processing via Energy Relaxation

As inference-time steering methods like EmbedOpt and DPS can push samples off from the original model’s manifold, the generated structures may exhibit local steric clashes or other geometry inconsistencies. To address this issue, we apply a physics-based energy relaxation as a post-processing step, following prior work (Maddipatla et al., 2025). More specifically, after sample generation from EmbedOpt or DPS, each structure is completed with hydrogen atoms and locally relaxed via energy minimization under a classical AMBER force field (Ponder & Case, 2003).

Empirically, we find this step to be computationally lightweight. For most settings of EmbedOpt and DPS, applying energy relaxation produce physically plausible structures while largely preserving the experimental constraints, with only a small decrease in the corresponding reward value. However, for some settings, notably DPS with a large learning rate α (Figure 6), energy relaxation is insufficient to repair the resulting globally broken geometry.

D.2. Cryo-EM Map Fitting Benchmark

Forward model. The differentiable forward model $V(\cdot)$ which renders a denoised structure x_0 to a map $V(x_0)$ is implemented with SFC_Torch (Li et al., 2025). We first compute the structure factors $\mathbf{F}(\vec{h})$ in the frequency domain by summing the scattering contributions of individual atoms:

$$\mathbf{F}(\vec{h}) = \sum_j O_j \cdot f_{\vec{h},j} \cdot \text{DWF}(\vec{h}) \cdot \exp \left[2\pi i \vec{h} \cdot \vec{x}_j \right] \quad (44)$$

where j indexes the atoms, O_j denotes occupancy (fixed at 1.0), and \vec{x}_j represents the fractional coordinates. The term $f_{\vec{h},j}$ is the atomic scattering factor approximated via a 5-parameter Gaussian expansion (Prince, 2004), and DWF(\vec{h}) is the Debye-Waller factor corresponding to a uniform atomic B-factor of 50 \AA^2 . To match the target map properties, a high-frequency resolution cutoff (5.0 \AA) is applied in Fourier space, followed by an inverse FFT to recover the real-space voxel intensities on the target grid.

D.3. Distance-Constrained Structure Determination Benchmarks

Forward model. We define the constraint set by identifying the atomic indices of the top $K = 20$ residue pairs that exhibit the largest distance deviation between the unguided prior predictions and the ground truth PDB structure. The forward

operator is then defined as the computation of the pairwise Euclidean distances for these specific atomic indices from the denoised structure x_0 .

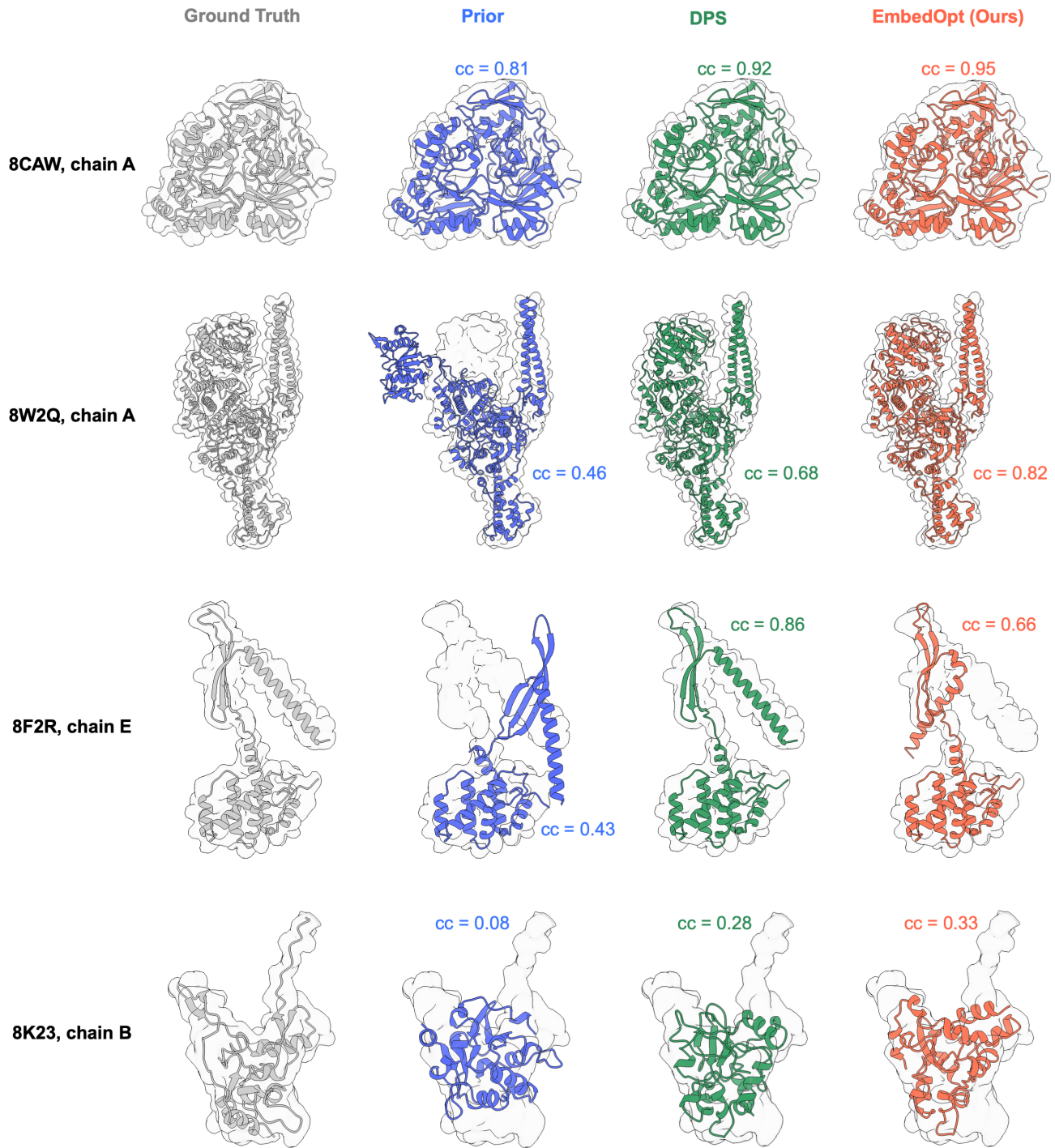


Figure 5. Cryo-EM Map Fitting Benchmark: Sample Gallery of Representative Results across Test Systems (Hyperparameter-Tuned). Structures display the best samples from each method following hyperparameter sweeping. Both methods perform robustly on targets where the unguided prior is already well-aligned with the target map (e.g., 8CAW). However, for targets requiring significant global conformational rearrangement (e.g., 8W2Q), EmbedOpt consistently achieves higher map correlation. We note 8F2R as the unique outlier where DPS significantly outperforms EmbedOpt, and 8K23 as a failure case where neither method successfully recovers the target structure.

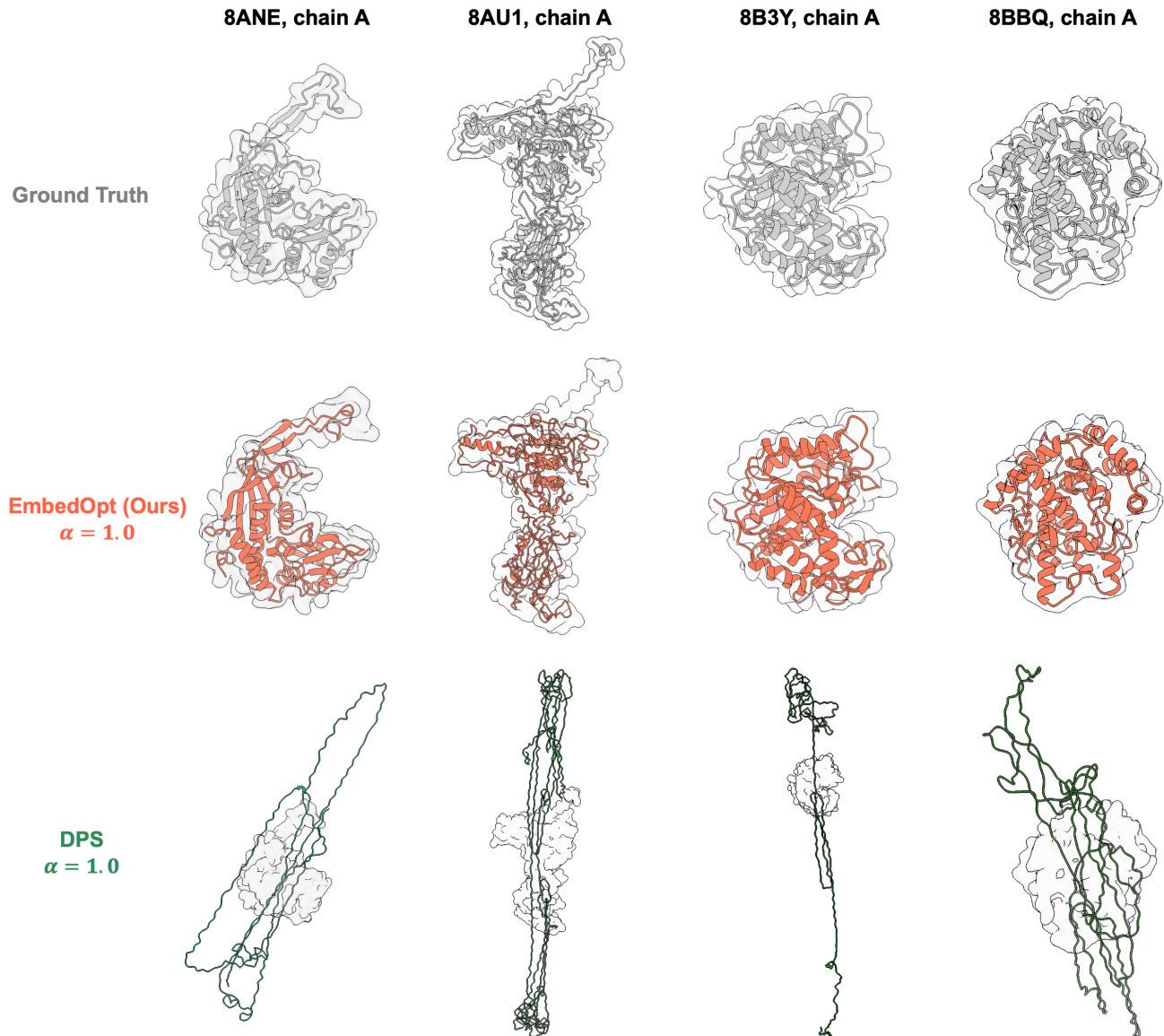


Figure 6. Cryo-EM Map Fitting Benchmark: Sample Gallery of EmbedOpt and DPS Failure Modes under High Learning Rates. We visualize the impact of high learning rates ($\alpha=1.0$) on generation quality for both methods. DPS (bottom) that directly steers noisy coordinates can push trajectories off the data manifold, resulting in unphysical, unraveled structures that defy energy relaxation. In contrast, EmbedOpt (middle) remains structurally coherent even in this aggressive regime.

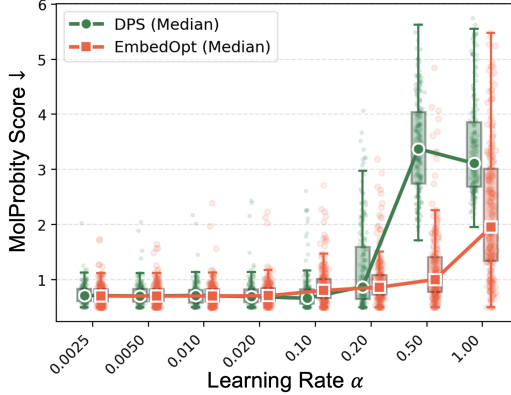


Figure 7. Cryo-EM Map Fitting Benchmark: Stereochemical Quality Analysis. Comparison of MolProbity scores (lower is better) across varying learning rates. EmbedOpt preserves structural validity even at high learning rates, whereas DPS suffers from severe geometric degradation when $\alpha > 0.1$.

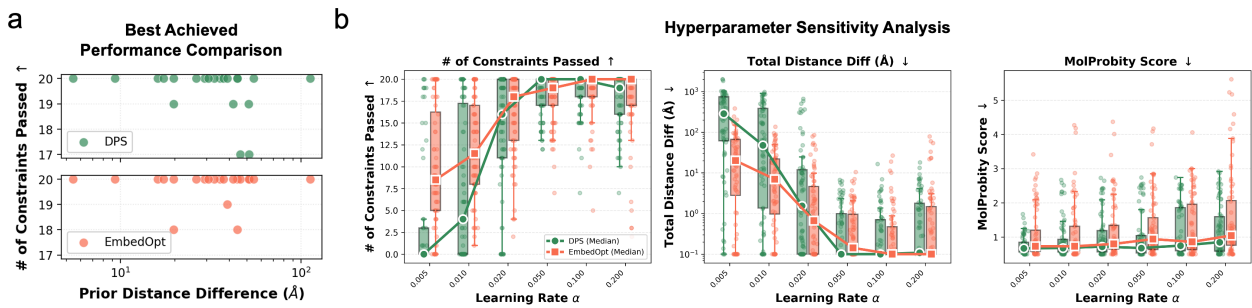


Figure 8. Distance-Constrained Structure Determination Benchmark: Performance Analysis. (a) **Best-Achieved Performance:** Comparison of constraint satisfaction on the $K = 20$ constraint benchmark, where systems are ordered by task difficulty (initial deviation between prior and target distances per constraint). Unlike the unimodal likelihood in Cryo-EM task, sparse constraints allow both methods to achieve comparable peak performance, with both satisfying all constraints for the majority of targets. (b) **Hyperparameter Sensitivity:** Metric distributions across varying learning rates (α) and fixed 200 steps for # of Constraints Passed (left, higher is better), Total Distance Violation (middle, lower is better), and MolProbity Score (right, lower is better). EmbedOpt (orange) demonstrates better robustness, maintaining high constraint adherence and valid geometries (low MolProbity scores) across a broad learning rate spectrum. Box plots denote the interquartile range (IQR) with median bars; whiskers extend to $1.5 \times$ IQR. Medians are highlighted.